Version 1.3

Spectroscopy and electronic structure of the low-energy states of ThN

Joel R. Schmitz and Michael C. Heaven*
Department of Chemistry
Emory University
Atlanta, GA 30322

Abstract

The electronic spectrum of ThN over the range 19600 – 21200 cm^{-1} is remarkably congested, showing at least twenty vibronic bands originating from the ground state zero-point level. Rotationally resolved spectra for eleven of these bands have been examined to probe the underlying reasons for the dense manifold of states. Dispersed fluorescence spectra and fluorescence decay lifetimes were also measured to provide addition insights. The experimental measurements were complemented by electronic structure calculations for the low-energy doublet and quartet states. The *ab initio* calculations yielded a density of excited states that was consistent with the congested spectrum. These states were derived from the formal configurations $Th^{3+}(6d)N^{3-}$, $Th^{2+}(7s^2)N^{2-}(2p^5)$ and $Th^{2+}(7s6d)N^{2-}(2p^5)$. The calculations indicated that the rotational and vibrational constants would be characteristic of the electronic configurations. This prediction was not borne out by the experimental data, suggesting that the full range of inter-configurational state interactions were not captured by the computational model.

*Corresponding author. E-mail: mheaven@emory.edu, Phone: 404 727 6617, FAX 404 727 6586

Introduction

The electronic structure of diatomic ThN has been examined in previous studies that employed electronic excitation and microwave spectroscopy techniques[1, 2]. *Ab initio* electronic structure calculations were also used to examine the properties of the $X^2\Sigma^+$ ground state and several low-lying electronically excited states[1]. The first gas phase observations of ThN were made using the resonantly enhanced multi-photon ionization (REMPI) technique, with mass-resolved ion detection. This had the advantage of excluding the ubiquitous interference from the ever-present ThO[3]. A survey spectrum for ThN recorded in the 19700 – 21200 cm^{-1} range (reproduced in Fig. 1) revealed a large number of optically active vibronic bands (>20). As the ThN sample was cooled by supersonic jet expansion, almost all of the bands evident in Fig. 1 originated from the ground state zero-point level. Rotational resolution of the stronger bands indicated the common occurrence of local perturbations of the excited states, and confirmed the expected $X^2\Sigma^+$ assignment for the ground state. This was consistent with the formal $Th^{3+}(7s)N^{3-}$ configuration, where the unpaired electron resides in the mostly non-bonding Th 7*s* orbital.

High-resolution data for ThN were obtained by means of laser-induced fluorescence (LIF) and microwave-optical double resonance techniques[2]. A relatively unperturbed band at 18005 cm^{-1} ([18.0]3/2-$X^2\Sigma^+$) was used for these measurements. Electric dipole moments and magnetic *g*-factors were derived from measurements of the Stark and Zeeman level splittings. The ground state exhibited a dipole moment of 5.11(9) D and the Zeeman splittings were consistent with the *g*-factor for a free electron (g=2.002). Microwave data yielded rotational constants, spin-rotation terms and ^{14}N hyperfine interaction constants. The zero-point average bond length was found to be R_0=1.82222 Å.

Multi-reference configuration interaction calculations with spin-orbit coupling (MRSDCI+Q/SO, defined below) were used to explore configurational assignments for the electronically excited states[1]. Qualitatively, the predicted pattern of energy levels was consistent with a ligand field theory (LFT) model[4, 5]. The first families of excited levels were found above 10000 cm^{-1} and they were derived from the metal-centered excited configuration $Th^{3+}(6d)N^{3-}$, and formally charge transfer states of the type $Th^{2+}(7s^2)N^{2-}(2p^5)$ and $Th^{2+}(7s6d)N^{2-}(2p^5)$. The large number of states arising from these configurations (collected in Table 1) may account for the density of states observed in Fig. 1. Neither multi-reference quantum

calculations nor LFT models are, at the present time, capable of providing individual state assignments for the bands of Fig. 1. However, LFT predicts that the families of states arising from a specific configuration should exhibit similar molecular properties that are characteristic (e.g., vibrational frequencies and rotational constants)[4-6]. This suggests that we may be able to identify groups of states within the spectrum shown in Fig. 1 that can be linked by common molecular properties. The congestion and erratic band spacings of Fig.1 prevent the assignment of upper state vibrational quantum numbers, but it may be possible to derive this information from the intensity contours of wavelength dispersed laser induced fluorescence (DLIF) spectra. Rotational constants and fluorescence decay lifetimes could also be useful for establishing configurational assignments.

In the present study we have recorded new spectra for many of the bands of Fig. 1 using the technique of LIF, as this yields better resolution than REMPI in the spectrometer that was used for the first measurements[1] (the primary limitation being that we did not examine bands that were overlapped by strong transitions of ThO). For most of the bands we also recorded DLIF spectra and fluorescence decay lifetimes. To facilitate the interpretation of these data we performed new electronic structure calculations for the excited states of ThN. The primary objective of the calculations was to estimate characteristic molecular constants and provide data for the low-energy quartet states, that were not considered in earlier calculations.

Experimental

Thorium nitride (ThN) was produced using similar supersonic expansion techniques to those detailed by Bresler *et al.*[7]. Vaporized thorium was produced by focusing the pulses from an Nd:YAG laser (10 mJ / pulse at 1064 nm) onto a thorium rod (International Bio-Analytical Industries Inc.). To ensure consistent ablation, the thorium rod was continuously rotated and translated. The thorium vapor was seeded in a 1% NH_3/He gas mixture supplied by a Parker Hannifin General Valve (Series 9) with a pulse duration of 390 μs. The backing pressure was 120 psi and the resulting gas mixture was supersonically expanded through a 3 mm diameter orifice.

The ablation products were probed using a pulsed dye laser (Lambda-Physik, FL 3002e) pumped by a XeCl excimer laser (Lambda-Physik, Complex Pro 201) with a pulse duration of 10 ns and a FWHW linewidth of 0.3 cm^{-1}. For the recording of rotationally resolved spectra, an

intracavity etalon was used to reduce the linewidth to 0.06 cm^{-1}. Fluorescence emitted perpendicular to the propagation axis of the probe laser was collimated and focused outside of the chamber onto a photomultiplier tube (PMT, Hamamatsu R955). To reduce scatter from the dye laser, a long-pass filter with a cut-on wavelength approximately 20 nm longer the dye laser wavelength was used to shield the PMT. The signal from the PMT was sent to both an oscilloscope (Tektronix TDS 2014) and a boxcar integrator (Stanford Research Systems, SRS 250). For lifetime measurements, the fluorescence decay curve was signal averaged for 32 laser pulses and then downloaded directly from the oscilloscope. Background measurements were taken without the dye laser entering the chamber and were then subtracted from the fluorescence decay curves to correct for the chemiluminescence of the ablation products.

To record LIF spectra, voltage readings from the boxcar were digitized by a National Instruments Data Acquisition Device (NI DAQ) which was also used to step the dye laser in 0.003 nm increments and record 30 averages at each wavelength step.

For absolute wavenumber calibration, a sealed cell containing ^{130}Te was heated in an oven to 650°C to produce a sufficient vapor pressure of Te_2. After passing through the vacuum chamber, the dye laser beam was directed through the cell. A photodiode was used to detect $^{130}Te_2$ absorbance, averaging 30 laser pulses for each wavelength step. Absorption spectra were fit to the line positions of a standard spectral atlas[8] for Te_2.

For dispersed laser-induced fluorescence (DLIF) measurements, the LIF was focused through the entrance slits a 0.64m monochromator equipped with a 1200 groves/mm diffraction grating. Light exiting the monochromator was detected by a PMT. DLIF spectra were taken by exciting the most intense rotational feature of the desired vibronic transition and then scanning the monochromator by using a stepper motor to drive the diffraction grating. The monochromator was swept over the spectral range from the resonant transitions to 8000 cm^{-1} lower than the excitation photon energy. Relative emission intensities were adjusted to compensate for the wavelength dependent PMT efficiency. Referring to the Hamamatsu R955 PMT datasheet, values of the cathode radiant sensitivity of the PMT at wavelengths ranging from 400-800 nm were fit to a cubic function which was then applied to the DLIF emission intensities.

Results and analyses

Rotationally resolved spectra were recorded for 11 bands (10 of which are marked with asterisks in Fig. 1). Figure 2 shows the rotational structure of a band centered near 20605 cm^{-1}. The downward-going trace in this figure is a simulation generated using the PGOPHER software package[9]. The ground state molecular constants for this simulation were fixed at the values determined by Le *et al.*[2] ($B_0^{"} = 0.38462$, $D_0^{"} = 2.49 \times 10^{-7}$, $\gamma_0^{"}$=0.016399 cm^{-1}), and the rotational energies determined by the expressions[10],

$$F_1^{"}(J^{"}) = B_0^{"}(J^{"} - 1/2)(J^{"} + 1/2) - D_0^{"}((J^{"} - 1/2)(J^{"} + 1/2))^2 + \gamma^{"}(J^{"} - 1/2)/2 \qquad (1)$$

$$F_2^{"}(J^{"}) = B_0^{"}(J^{"} + 1/2)(J^{"} + 3/2) - D_0^{"}((J^{"} + 1/2)(J^{"} + 3/2))^2 - \gamma^{"}(J^{"} + 3/2)/2 \qquad (2)$$

The upper state was treated as a Hund's case (c), Ω=3/2 state. This constraint was imposed on the PGOPHER model by setting the upper state term symbol to $^2\Pi$ and selecting the Ω-component. Owing to the relatively low resolution of the spectra, only the upper state vibronic term energy (T_0') and the rotational constant (B') could be determined with statistical significance. Using these variables and the above method for constraint to Hund's case (c), the effective expressions for the upper state energies were

$$E'_{3/2}(J') = T_0' + B'((J' + 1/2)^2 - 1) \qquad \text{for} \quad \Omega\text{'=3/2} \qquad (3)$$

and

$$E'_{1/2}(J') = T_0' + B'((J' + 1/2)^2 + 1) \qquad \text{for} \quad \Omega\text{'=1/2} \qquad (4)$$

The rotational temperature used in the simulation for Fig. 1 was 90 K, and the spectra typically exhibited temperatures in the 40-90 K range. Eight bands were found to be relatively unperturbed, yielding acceptable fits to the given energy level expressions with the assumption that they all originate from the ground state zero-point level. The constants resulting from these fits are collected in Table 2, where we have also included the results for the [18.00]3/2-X$^2\Sigma^+$ band that were reported in ref. [2]. Note that the definition of T_0' used in the present work differs from that of ref. [2] by an offset of B' (T_0'(present)= T_0' (ref. [2])- B').

Three bands that showed obvious local perturbations were also modeled using the PGOPHER software. Two of the excited states were treated as being Hund's case (c) $^2\Pi_{1/2}$ states and the third was modeled as a $^4\Sigma^+$ state. The perturbed bands could be adequately reproduced by assuming that the perturbing interactions were of kind $^2\Pi_{1/2} \leftrightarrow {}^2\Sigma^-$ (mediated by the $\hat{J}^{\pm}\hat{L}^{\mp}$ operators) and $^4\Sigma^+ \leftrightarrow {}^4\Sigma^+$ (mediated by $\hat{J}^{\pm}\hat{S}^{\mp}$). As an example, Fig. 3 shows the perturbed

band at 20196.6 cm^{-1} with the best fit simulation. Molecular constants derived from fitting to the perturbed bands are listed in Table 3.

Fluorescence decay curves were recorded for most of the excited states reported here. These data were taken with the dye laser set to excite the most intense feature of each band (usually the R-branch band head). In all cases the temporal behavior was consistent with a single exponential decay process. The fluorescence decay lifetimes are listed in Tables 2 and 3.

DLIF spectra were recorded using excitation of nine of the rotationally resolved bands, and two other vibronic transitions that were only studied at low resolution (20679 and 21055 cm^{-1}). The DLIF spectra were obtained in the visible spectral range, running out to a long-wavelength limit of approximately 860 nm (limited by the falling PMT response). Based on the electronic structure calculations presented in ref. [1], it was expected that only transitions to the ground state would be observed. Fig. 4 shows a composite plot of the DLIF spectra, scaled so that the ground state vibrational energy defines the x-axis origin. The results are clearly consistent with simple progressions of the ground state vibrational levels. Previous DLIF measurements had revealed only the $v^{"}$=0 and 1 levels, so that $\Delta G^{"}_{1/2}$ was the only vibrational interval that could be determined. The present spectra show levels up to $v^{"}$=8, with vibrational energies that are well represented by the simple Morse expression

$$G(v^{"}) = \omega^{"}_e(v^{"} + 1/2) - \omega_e x^{"}_e(v^{"} + 1/2)^2 \quad (5)$$

Fitting this expression to the observed energies yielded $\omega^{"}_e$=962±4 and $\omega_e x^{"}_e$=4.43±0.42 cm^{-1}.

Electronic structure calculations for ThN

Previous electronic structure calculations for ThN considered just the lowest energy doublet states[1]. In the calculations presented here we have increased the number of excited states included, and performed calculations for the low-energy quartet states.

Each sequence of calculations began with the restricted Hartree-Fock model to generate starting orbitals. This was followed by state-averaged complete active space self-consistent field (SA-CASSCF) calculations. Dynamical weighting was implemented using the parameter value DYNW=2. Configuration interaction (CI) was then included using the multi-reference single and double excitation CI method with inclusion of the Davidson correction (MRSDCI+Q). Finally, the spin-orbit interaction was taken into account by diagonalizing the matrix of the Breit-Pauli operator constructed in the SA-CASSCF eigenbasis. In this procedure, the spin-free energies of

the MRSDCI+Q calculations were used in the diagonal matrix elements. The ECP60MWB_ANO basis set was used for Th[11, 12], with exclusion of the *g*-orbitals. The aug-cc-pVTZ basis set was used for N[13]. All electronic structure calculations were carried out using the Molpro2015.1 suite of programs[14], where the orbitals were symmetry adapted using the C_{2v} point group (the highest available symmetry provided for a heteronuclear diatomic). The active space consisted of eight molecular orbitals ($3a_1 \oplus 2b_1 \oplus 2b_2 \oplus a_2$) constructed from the Th 7*s* and 6*d* and N 2*s* and 2*p* orbitals. The calculations included 14 spin-free doublet states ($5a_1 \oplus 3b_1 \oplus 3b_2 \oplus 3a_2$) and 16 spin-free quartet states ($4a_1 \oplus 4b_1 \oplus 4b_2 \oplus 4a_2$). The validity of the SA-CASSCF calculations was supported by the integer values obtained for the expectation values of the $\hat{L}_z^2$ operator. The doublet and quartet states were examined in separate calculations, so the results did not include spin-orbit mixing between the spin manifolds.

Potential energy curves were constructed by performing single-point energy calculations for a range of internuclear distances. Typically, the range was chosen to run from 1.66 to 2.20 Å in steps of 0.04 Å. Molecular constants were obtained by fitting Morse potential energy functions to the single point energies. Fig's 5 and 6 show the potential energy curves for the doublet and quartet states, respectively. Table 4 provides representative molecular constants. From inspection of Fig. 5 it can be seen that the pattern of low-energy doublet states is consistent with expectations based on LFT (as noted previously in ref. [1]). Near the ground state equilibrium distance, the first three states ($X^2\Sigma^+$, $1^2\Delta_{3/2}$, $1^2\Delta_{5/2}$) are derived from the $Th^{3+}N^{3-}$ configuration. Characteristically, they exhibit the shortest equilibrium bond distances and highest vibrational frequencies (c.f. Table 4). For the next group of states the equilibrium distances has shifted out to approximately 2 Å and the vibrational frequencies drop to values near 740 cm^{-1}. These states are derived from the $Th^{2+}N^{2-}$ configuration, with the lowest energy pair being the $1^2\Pi_{1/2}$ and $1^2\Pi_{3/2}$ states of $Th^{2+}(7s^2)\,N^{2-}(2p^5)$. At higher energy there are several closely similar potential energy curves that are derived from $Th^{2+}(7s6d)\,N^{2-}(2p^5)$. The ordering of electronic states for the ground state equilibrium distance is given in Table 5, along with Hund's case (a) labels for the states that report the basis functions that make the leading contributions. As there are many state interactions, the basis function contributions change significantly with increasing internuclear distance over the range examined.

Comparing Fig's 5 and 6 it is apparent that the lowest energy quartet states have potential energy curves that are very similar to the doublet potential energy curves for the low energy

states of $Th^{2+}N^{2-}$. This is not surprising as the lowest energy configuration that can support a quartet state is $Th^{2+}(7s6d)\,N^{2-}(2p^5)$. Representative molecular constants for the quartet states are included in Table 4 The lowest energy state has a term energy of 14788 cm^{-1} and there are many quartet states that fall in the energy range probed in the REMPI and LIF spectroscopy experiments.

Discussion

The predicted density of excited states for ThN is sufficient to account for the congested spectrum shown in Fig. 1. The calculations also support the expectation that an ionic model of the bonding (LFT) can be used to anticipate the families of low-lying electronically excited states (e.g., Table 1). A*b initio* calculations for these families of states yielded molecular constants that were characteristic of the underlying electronic configuration. Consequently, we have examined the results from the present spectroscopic study for distinguishable groupings of constants that would provide some insight concerning the configurational origin of each excited state.

Regular vibrational intervals were not apparent in the spectrum, which complicates the determination of the upper state vibrational assignments. The DLIF spectra did not prove to be as helpful in assigning vibrational states as we had hoped. Spectra recorded with excitation of the 19946, 20679, 20937, 20969 and 21055 cm^{-1} bands had intensity distributions that indicated v'=0 upper states. The other states examined showed fluorescence transitions that radiated down to a range of ground state vibrational levels. These upper levels may have been vibrationally excited or they may be v'=0 levels that are significantly perturbed. Fluorescence decay lifetime measurements also yielded ambiguous results. As can be seen in Tables 2 and 3, the lifetimes were dependent on the excited state, but there were no systematic trends. States that were clearly perturbed exhibited lifetimes that were within the range of values observed for the states that were not obviously perturbed. Similarly, states with qualitatively different DLIF spectra did not show characteristic lifetime differences.

Rotational constants provide another possible flag for the electronic configuration. The *ab initio* calculations reported here indicate that excited states that have the formal $Th^{2+}N^{2-}$ configuration will have rotational constants slightly below 0.32 cm^{-1}. Most of the rotational constants recovered from the spectra were larger than this, but lower than the $Th^{3+}N^{3-}$ value that was close to 0.38 cm^{-1}. Taking the simplest model, it might be anticipated that excited states that yielded long vibrational progressions in the ground state would have smaller rotational constants.

This expectation was also not supported. For example, the 20604 cm^{-1} state, which has a strong emission down to v''=4, has a rotational constant of B' =0.3487 cm^{-1}.

Overall, the lack of systematic trends for the excited state properties of ThN indicates extensive state mixing that no doubt involves both the doublet and quartet spin manifolds. Dipole moment and magnetic *g*-factors provide other flags for configurational assignment[15-18], but it seems likely that the information obtained will be subject to similar ambiguities. For example, Le *et al.*[2] found that the magnetic *g*-factor of the [18.0]3/2 state was consistent with assignment to a case (a) $^2\Pi_{3/2}$ state, but this interpretation required the assumption that this was a doublet state, and did not yield configurational insights. Measurements of the electric dipole moments for the [18.0]3/2 and $X^2\Sigma^+$ states yielded values of μ=4.38 and 5.11 D, respectively. In a first-order model, the change in the dipole moment on excitation could indicate a charge-transfer transition but the rotational constant for the [18.0]3/2 state (0.3523 cm^{-1}) is significantly larger than the constants predicted for the charge transfer states, and the change in the dipole moment is smaller than the *ab initio* predictions ($\Delta\mu$>2D). This suggests the presence of state mixings that are not captured by the calculations performed in this study. Given the similar characteristics of the charge-transfer potential energy curves of the doublet and quartet states, it does not appear that mixing of these manifolds would resolve this shortcoming. It is evident that higher level calculations (e.g., inclusion of Th 6d in the active space), beyond the computational resources of the present study, will be needed to achieve a better understanding of the low-lying electronically excited states of ThN.

Acknowledgments

We thank Mr. Sean M. Bresler for his contributions in substantially improving the apparatus and LabVIEW programs that were used to record the LIF and DLIF spectra for ThN.

This research was support by the US Department of Energy under grant DE-FG02-01ER15153.

References

[1] M.C. Heaven, B.J. Barker, I.O. Antonov, J. Phys. Chem. A, 118 (2014) 10867-10881.

[2] A.T. Le, S.G. Nakhate, D.-T. Nguyen, T.C. Steimle, M.C. Heaven, J. Chem. Phys., 150 (2019) 144304/144301-144304/144309.

[3] J.R. Schmitz, L.A. Kaledin, M.C. Heaven, J. Mol. Spectrosc., 360 (2019) 39-43.

[4] R.W. Field, Ber. Bunsenges. Phys. Chem., 86 (1982) 771-779.

[5] L.A. Kaledin, A.L. Kaledin, M.C. Heaven, J. Comput. Chem., 40 (2019) 430-446.

[6] L.A. Kaledin, J.E. McCord, M.C. Heaven, J. Mol. Spectrosc., 164 (1994) 27-65.

[7] S.M. Bresler, J.R. Schmitz, M.C. Heaven, R.W. Field, J. Mol. Spectrosc., 370 (2020) 111293.

[8] J. Cariou, P. Luc, Atlas du Spectre d'Absorption de la Molecule de Tellure, CNRS, Paris, 1980.

[9] C.M. Western, J. Quant. Spectrosc. Radiat. Transfer, 186 (2017) 221-242.

[10] J.M. Brown, A. Carrington, Rotational Spectroscopy of Diatomic Molecules, 2003.

[11] X. Cao, M. Dolg, Theochem, 673 (2004) 203-209.

[12] X. Cao, M. Dolg, H. Stoll, Journal of Chemical Physics, 118 (2003) 487-496.

[13] T.H. Dunning, Jr., J. Chem. Phys., 90 (1989) 1007-1023.

[14] H.-J. Werner, P.J. Knowles, G. Knizia, F.R. Manby, M. Schuetz, Wiley Interdiscip. Rev. Comput. Mol. Sci., 2 (2012) 242-253.

[15] M.C. Heaven, V. Goncharov, T.C. Steimle, T. Ma, C. Linton, J. Chem. Phys., 125 (2006) 204314/204311-204314/204311.

[16] C. Linton, A.G. Adam, T.C. Steimle, J. Chem. Phys., 140 (2014) 214305/214301-214305/214307.

[17] D.-T. Nguyen, T. Steimle, C. Linton, L. Cheng, J. Phys. Chem. A, 123 (2019) 1423-1433.

[18] H. Schall, J.A. Gray, M. Dulick, R.W. Field, J. Chem. Phys., 85 (1986) 751-762.

Table 1. States arising from low-energy electronic configurations of ThN

Configuration	States
$Th^{3+}(7s)N^{3-}(2p^6)$	$^2\Sigma^+$
$Th^{3+}(6d)N^{3-}(2p^6)$	$^2\Sigma^+$, $^2\Pi$, $^2\Delta$
$Th^{2+}(7s^2)N^{2-}(2p^5)$	$^2\Sigma^+$, $^2\Pi$
$Th^{2+}(7s6d)N^{2-}(2p^5)$	$^2\Sigma^+(\times4)$, $^4\Sigma^+(\times2)$, $^2\Sigma^-(\times2)$, $^4\Sigma^-$, $^2\Pi(\times6)$, $^4\Pi(\times2)$, $^2\Delta(\times4)$, $^4\Delta$, $^2\Phi(\times2)$, $^4\Phi$

Table 2. Excited state molecular constants determined from unperturbed bands of ThN

$[T_0/1000]\Omega'$	v_0 (cm^{-1})	B' (cm^{-1})	γ' (cm^{-1})	Avg Res (cm^{-1})	τ / ns
[18.00]3/2	18005.0720[a]	0.352274	---	0.0004	---
[19.79]1/2	19789.2(1)	0.3224(5)	---	0.13	---
$[19.95]^2\Sigma^+_{1/2}$	19946.0(1)[b]	0.3352(5)	0.137(1)	0.05	281(4)
[20.18]3/2	20176.1(1)	0.3208(5)	---	0.09	462(7)
[20.58]1/2	20576.3(1)	0.3454(7)	---	0.10	317(3)
[20.60]3/2	20603.5(1)	0.3487(5)	---	0.04	220(3)
[20.74]1/2	20735.9(1)	0.322(2)	---	0.11	---
[20.94]3/2	20937.2(1)[c]	0.3190(5)	---	0.02	422(4)
$[20.97]\ ^2\Sigma^+_{1/2}$	20969.1(1)[b]	0.3328(5)	0.172(2)	0.06	743(2)

a. An initial analysis of this band was reported in ref. [1]
b. These bands were consistent with $^2\Sigma^+$ upper states with energy levels represented by Eq.'s 1 and 2.
c. Data from ref. [2]

Table 3. Excited state molecular constants determined from perturbed bands of ThN

Band Type	Ω'=1/2	Ω'=1/2	Ω'=3/2
T_0'	19655.1(1)	20196.6(1)	20542.1(1)
B'	0.34368	0.3349(1)	0.3492
γ'	-0.062	-	0.059
λ_{SS}	-	-	-0.74
Lifetime (ns)	289(2)	310(10)	265(11)
Perturbing state	$^2\Sigma^-$	$^2\Sigma^-$	$^4\Sigma^+$
$v_{0,p}$	19732.5	20197.7(1)	20550.1
B'_p	0.34	0.379(2)	0.33
Coupling term	$J^{\pm}L^{\mp}$	$J^{\pm}L^{\mp}$	$J^{\pm}S^{\mp}$
Coupling coefficient	0.05	0.05	0.02

Table 4 Calculated molecular constants for ThN

State	T_e	ω_e	$\omega_e x_e$	R_e	B_e
$X^2\Sigma^+$	0	956	3.8	1.82	0.385
$1^2\Delta_{3/2}$	10815	925	3.6	1.84	0.379
$1^2\Delta_{5/2}$	12110	929	3.6	1.83	0.380
$1^2\Pi_{1/2}$	14194	742	2.7	2.00	0.320
$1^2\Pi_{3/2}$	14669	738	2.8	2.00	0.320
$1^4\Pi_{1/2}$	14788	730	2.7	2.01	0.317
$1^4\Phi_{3/2}$	16537	728	2.8	2.01	0.317

All values are in units of cm^{-1} with the exception of R_e which is given in Å.

Table 5. Calculated doublet energy levels of ThN at an internuclear distance of R=1.82 Å

Configuration	State	Energy/cm^{-1}
$Th^{3+}(7s)N^{3-}(2p^6)$	X $1^2\Sigma^+$	0
$Th^{3+}(6d)N^{3-}(2p^6)$	$1^2\Delta_{3/2}$	10855
$Th^{3+}(6d)N^{3-}(2p^6)$	$1^2\Delta_{5/2}$	12141
$Th^{2+}(7s^2)N^{2-}(2p^5)$	$1^2\Pi_{3/2}$	18603
$Th^{2+}(7s^2)N^{2-}(2p^5)$	$1^2\Pi_{1/2}$	19258
$Th^{3+}(6d)N^{3-}(2p^6)$	$2^2\Sigma^+$	22832
$Th^{2+}(7s6d)N^{2-}(2p^5)$	$1^2\Phi_{5/2}$	25571
$Th^{2+}(7s6d)N^{2-}(2p^5)$	$2^2\Pi_{1/2}$	26575
$Th^{2+}(7s6d)N^{2-}(2p^5)$	$1^2\Phi_{7/2}$	26621
$Th^{2+}(7s6d)N^{2-}(2p^5)$	$2^2\Pi_{3/2}$	27303

Figure captions

1. ThN survey spectrum recorded using resonantly enhanced two-photon ionization. This spectrum is reproduced from ref. [1]. Ten of the bands examined in the present study are marked with asterisks. The eleventh band, centered at 19655 cm^{-1}, is not within this range.
2. Rotational structure of the $\Omega'=3/2 - X^2\Sigma^+$ band centered at 20605 cm^{-1}. The downward-going trace is a simulation carried out with an assumed rotational temperature of 90 K.
3. Rotational structure of the perturbed $\Omega'=1/2 - X^2\Sigma^+$ band centered at 19655 cm^{-1}. The downward-going trace is a simulation carried out with an assumed rotational temperature of 40 K.
4. Dispersed fluorescence spectra for ThN. The excitation photon energies are given in the left-hand column. Ground state vibrational levels are indicated across the top of the figure.
5. Calculated potential energy curves for the low-energy doublet states of ThN
6. Calculated potential energy curves for the low-energy quartet states of ThN

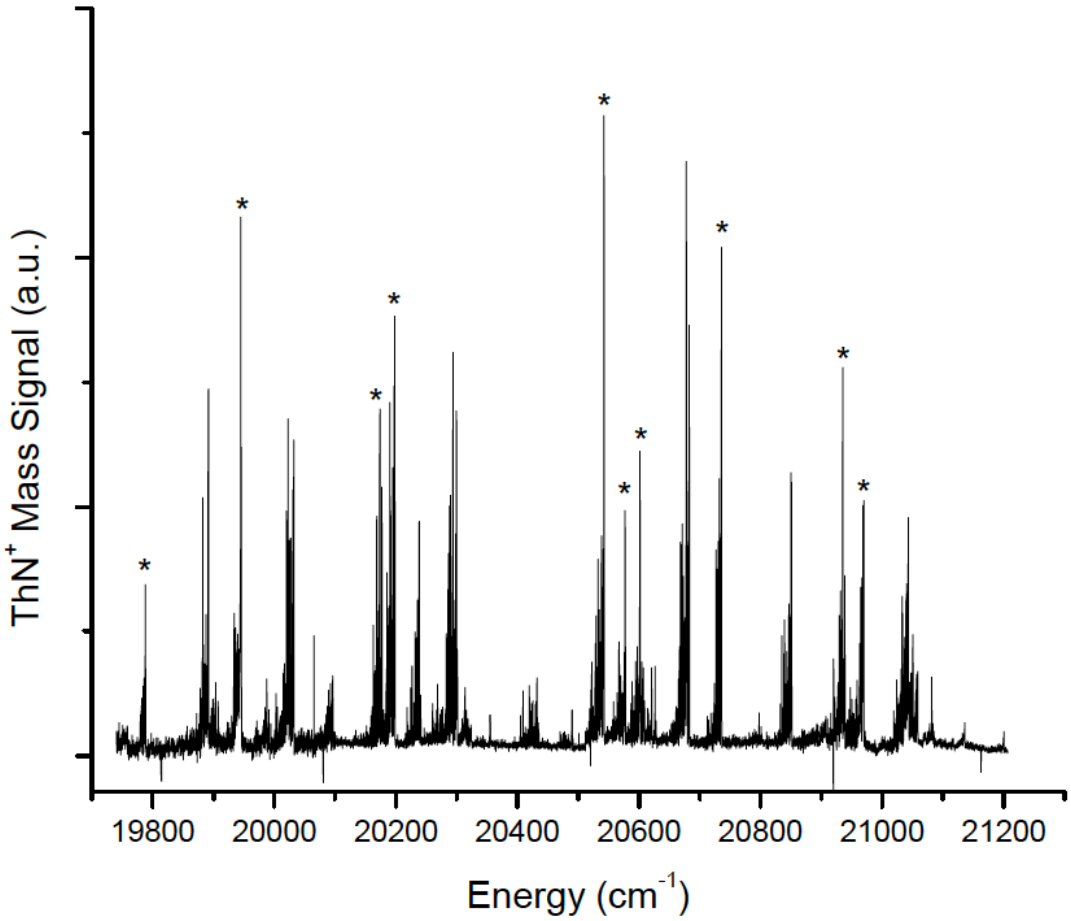
ThN+ Mass Signal (a.u.)
19800
20000
20200
20400
20600
20800
21000
21200
Energy (cm-1)

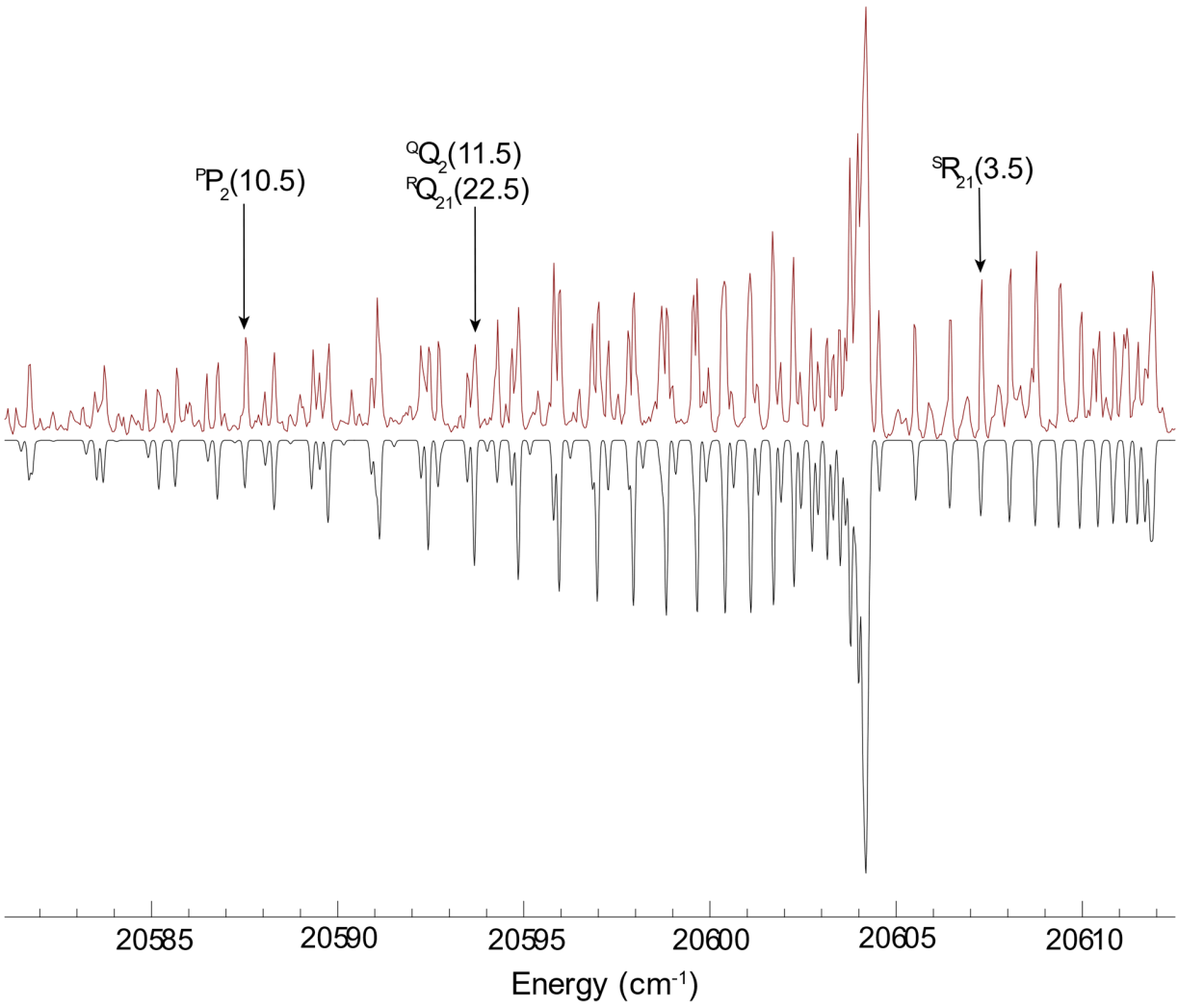
$^{P}P_2(10.5)$
$^{Q}Q_2(11.5)$
$^{R}Q_{21}(22.5)$
$^{S}R_{21}(3.5)$
20585
20590
20595
20600
20605
20610
Energy (cm^{-1})

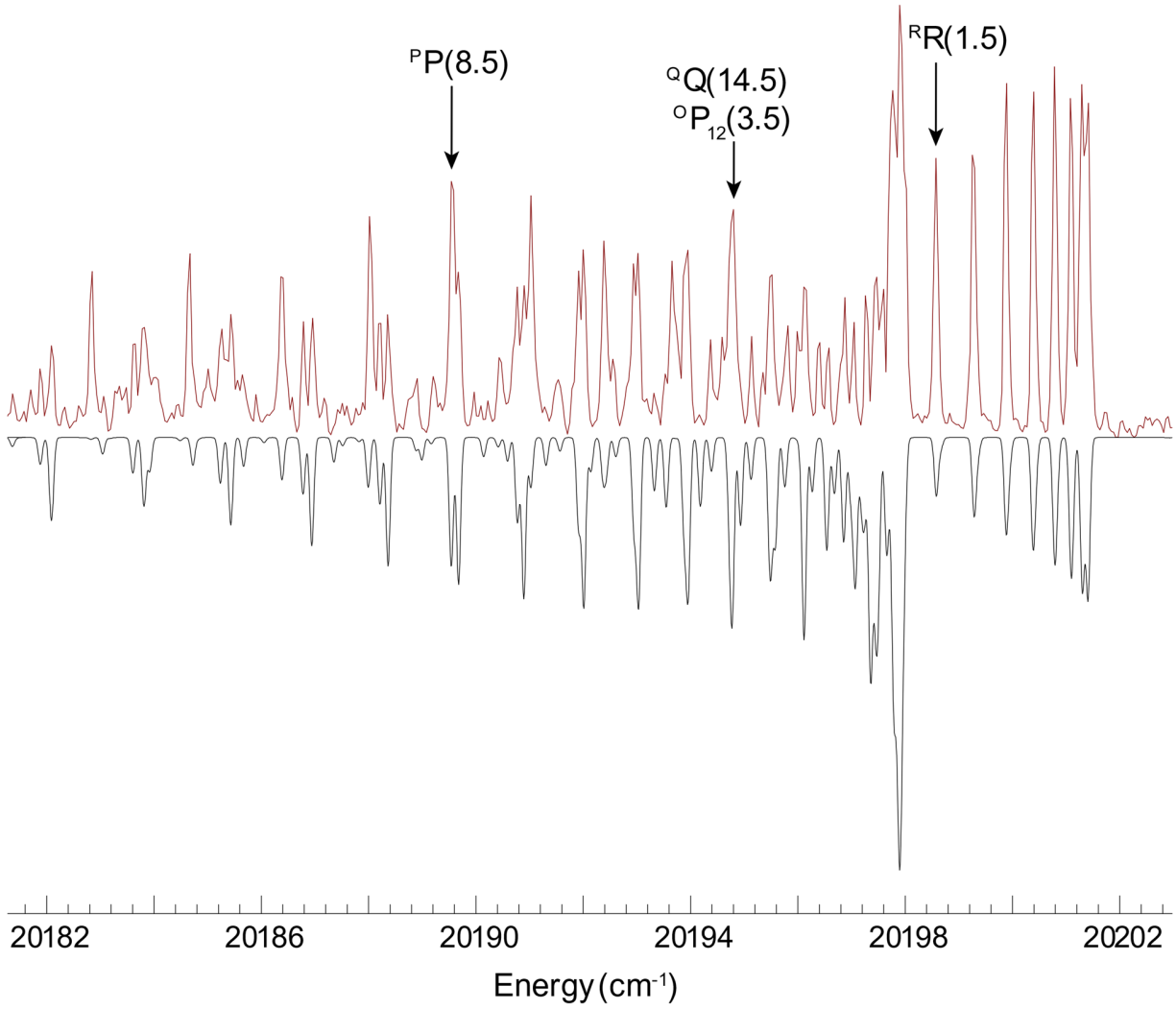
PP(8.5)
QQ(14.5)
OP12(3.5)
RR(1.5)
20182
20186
20190
20194
20198
20202
Energy (cm-1)

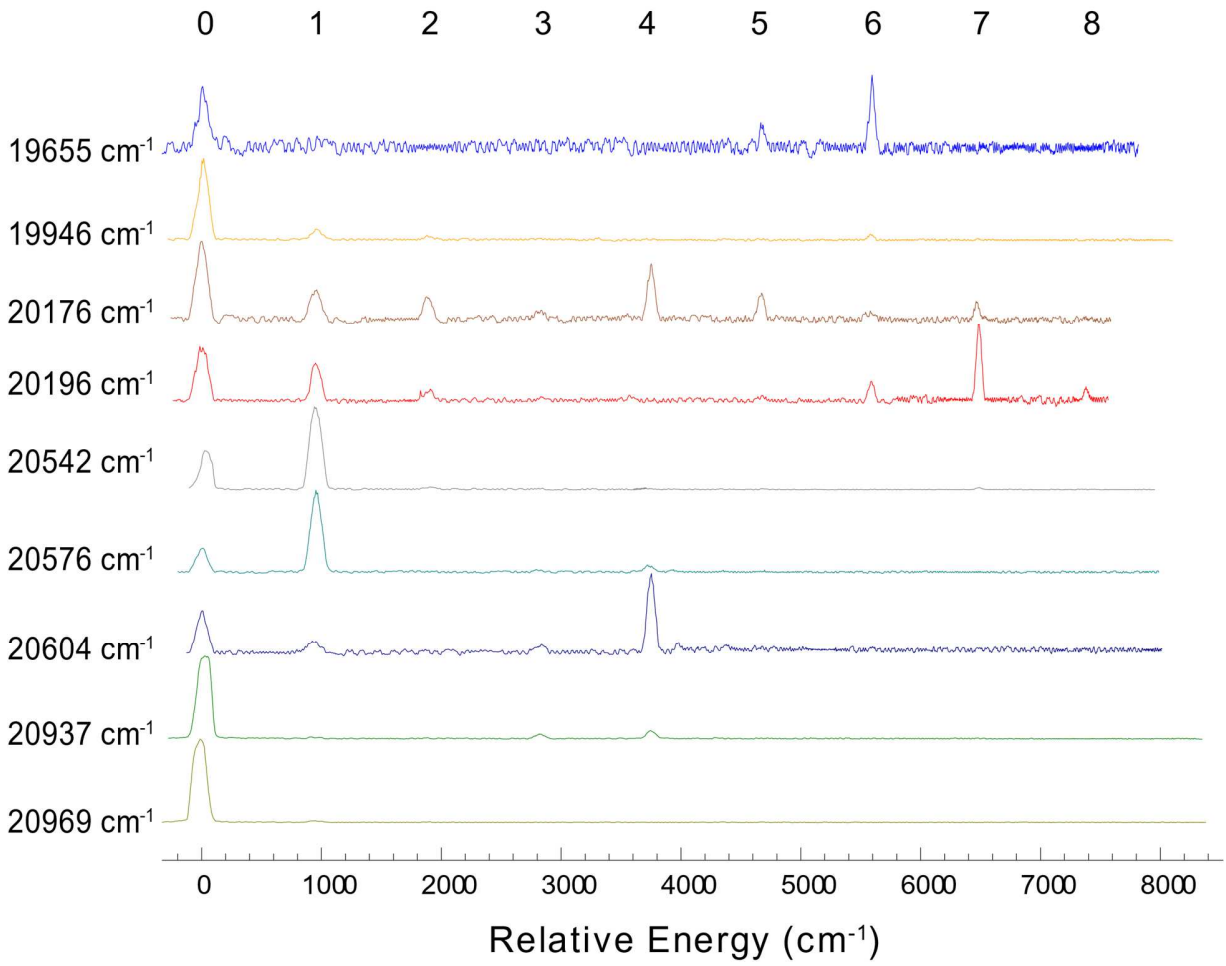
0
1
2
3
4
5
6
7
8
19655 cm-1
19946 cm-1
20176 cm-1
20196 cm-1
20542 cm-1
20576 cm-1
20604 cm-1
20937 cm-1
20969 cm-1
0
1000
2000
3000
4000
5000
6000
7000
8000
Relative Energy (cm-1)

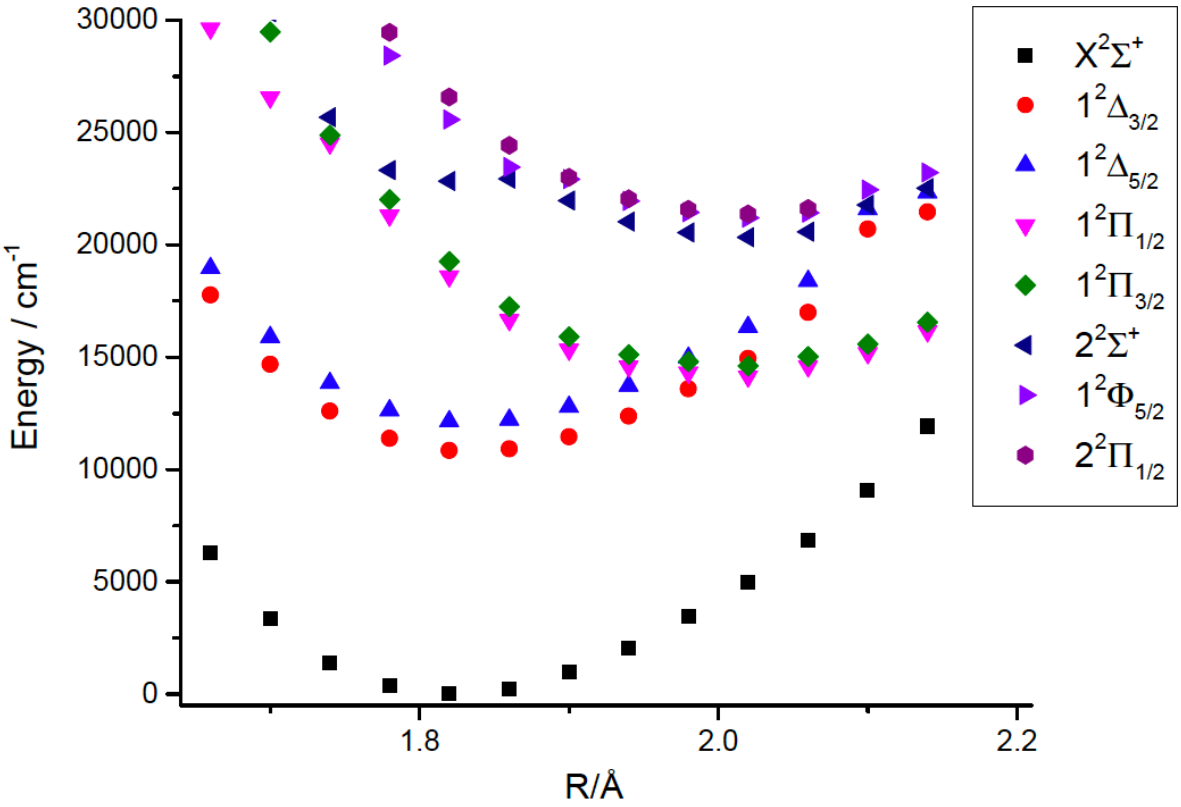
30000
25000
20000
15000
10000
5000
0
Energy / cm-1
1.8
2.0
2.2
R/Å
X2Σ+
1 2Δ3/2
1 2Δ5/2
1 2Π1/2
1 2Π3/2
2 2Σ+
1 2Φ5/2
2 2Π1/2

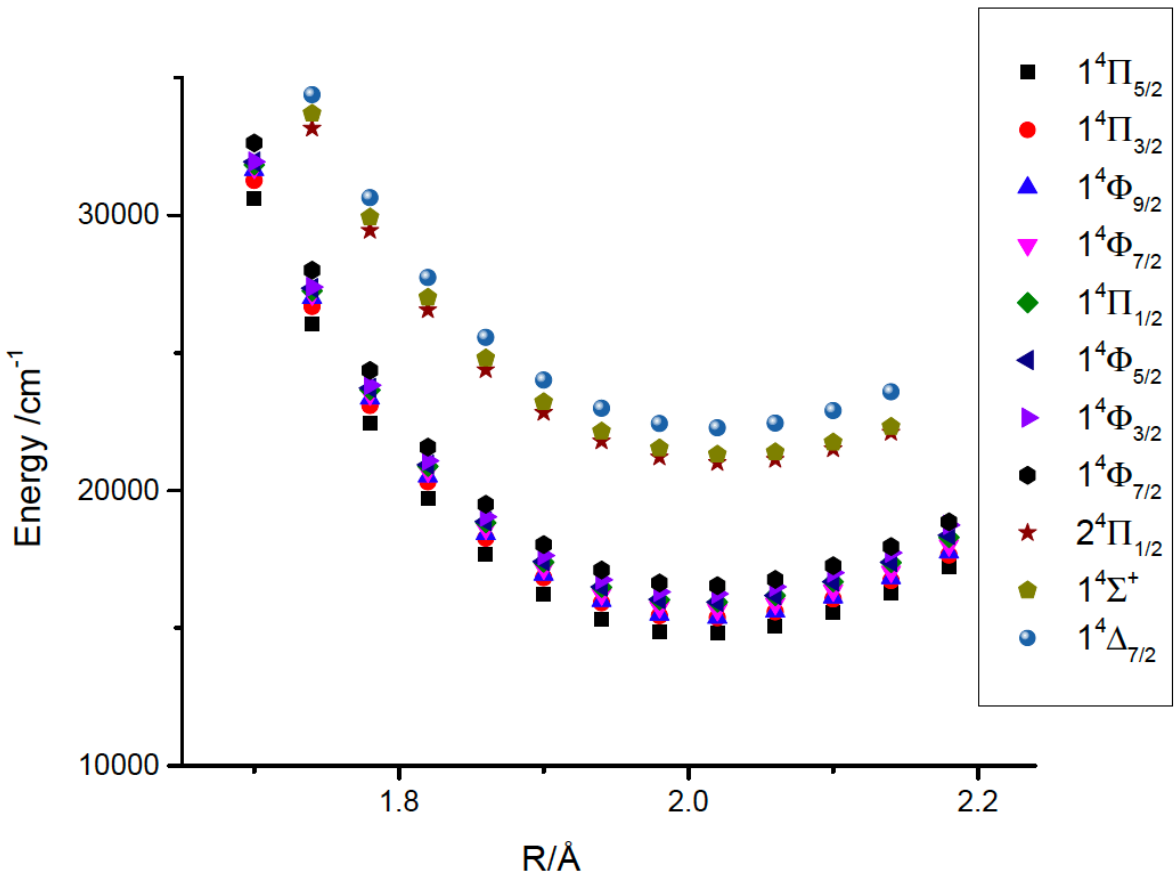
Energy /cm-1
30000
20000
10000
1.8
2.0
2.2
R/Å
1⁴Π5/2
1⁴Π3/2
1⁴Φ9/2
1⁴Φ7/2
1⁴Π1/2
1⁴Φ5/2
1⁴Φ3/2
1⁴Φ7/2
2⁴Π1/2
1⁴Σ+
1⁴Δ7/2

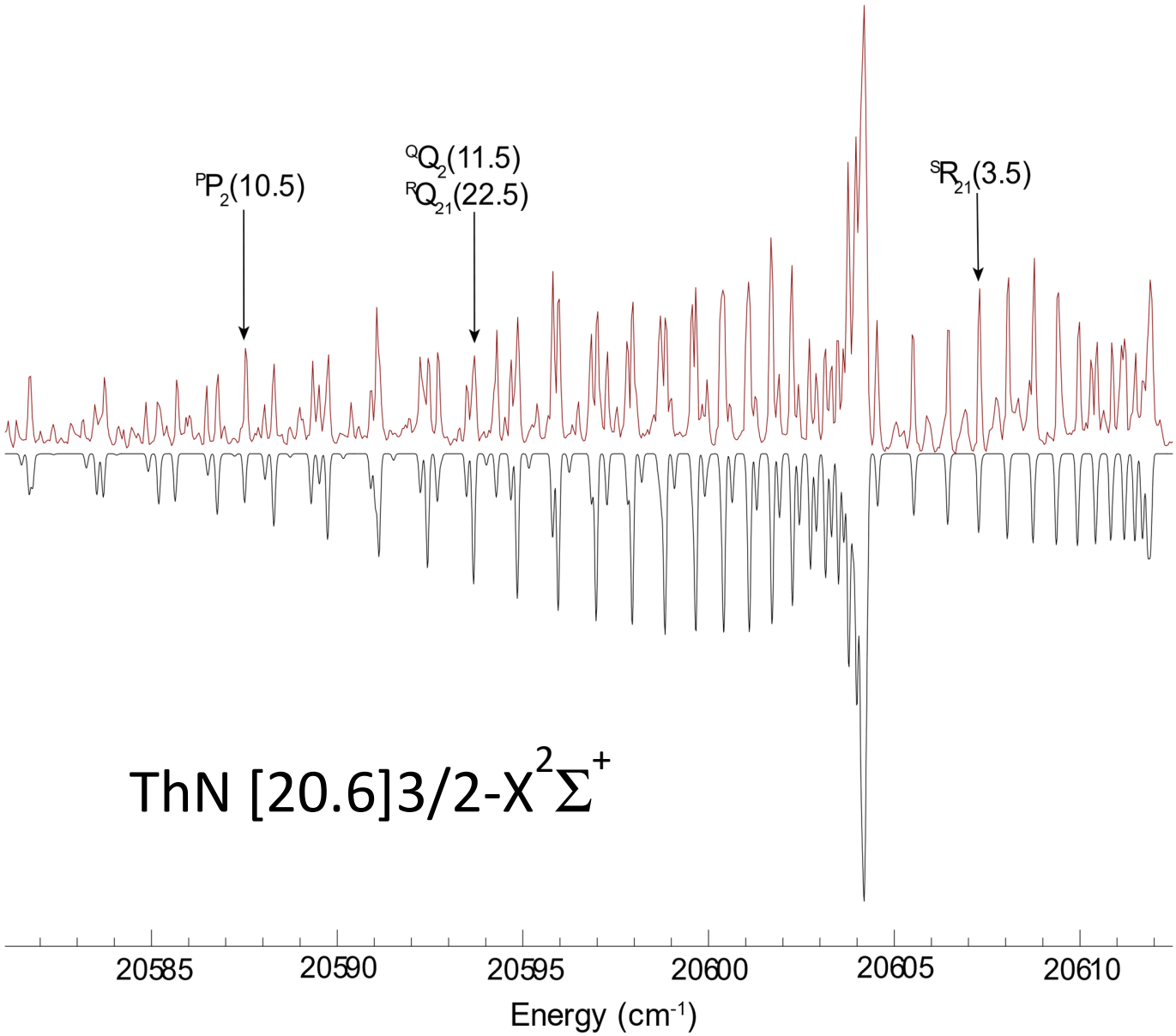
$^{P}P_2(10.5)$
$^{Q}Q_2(11.5)$
$^{R}Q_{21}(22.5)$
$^{S}R_{21}(3.5)$
ThN [20.6]3/2-$X^2\Sigma^+$
20585
20590
20595
20600
20605
20610
Energy (cm^{-1})